CrystEngComm

PAPER

View Article Online
View Journal | View Issue

Cite this: *CrystEngComm*, 2014, **16**, 1277

Controlled preparation of CdS nanoparticle arrays in amphiphilic perylene tetracarboxylic diimides: organization, electron-transfer and semiconducting properties†

Jingang Song,[a] Qingwen Tian,[a] Jian Gao,[a] Haixia Wu,[b] Yanli Chen*[a] and Xiyou Li*[b]

Received 30th September 2013,
Accepted 27th November 2013

DOI: 10.1039/c3ce41977k

www.rsc.org/crystengcomm

Langmuir monolayers of two amphiphilic perylene tetracarboxylic diimide (**PDI**) derivatives, **PDI-1** and **PDI-2**, which are modified with different numbers of hydrophilic polyoxyethylene/hydrophobic alkoxy side-chains, have been used as not only organic templates but also good functional organic materials to produce the first examples of rose- and petal-like nano-particle arrays of cadmium sulfide (CdS)–**PDI** composites with a controllable and tunable size (from 40, 60 to 80 nm for nano-roses; from 20 to 30 nm for nano-petals), respectively. These newly fabricated CdS–**PDI** hybrid nanostructures were comparatively studied using a wide range of methods including SEM, TEM, electronic absorption, fluorescence emission and X-ray diffraction analysis. The crystalline regions for CdS were identified to be hexagonal wurtzite with (101) and (001) face preferred growth on the **PDI-1** and **PDI-2** monolayers, respectively, associated with the polyoxyethylene side chains architecture changing from parallel to the subphase surface for **PDI-1** to perpendicular to the subphase surface for **PDI-2**. Furthermore, electron-transfer from **PDI** molecules to CdS nanocrystals is established by both quenching the photoluminescence intensity and changing the lifetime of photoluminescence emission of **PDI** in the hybrid nanoparticle arrays. In particular, a significantly enhanced conductivity for both nano-roses and nano-petals of CdS–**PDI** nanocomposites was achieved, relative to that of the individual component, due to the existence of the densely packed molecular architecture in the film matrix and the large interfacial area between the two components that removed the charge transporting bottleneck by creating an interpenetrating network of the hybrid materials, implying the potential of providing synergetic semiconducting properties of the present hybrid organic–inorganic nanomaterials.

Introduction

Facile approaches to fabricate semiconductor nanostructures have attracted scientists from different fields. Semiconductor nanomaterials can often display unique optical, electronic, and magnetic properties, whereas these properties strongly depend on the size and shape of the nanoparticles.[1,2] As a result, synthetic control over the morphology, size and crystallographic orientation of materials is highly desired.[3] Among the methods for the preparation of nanoscale materials, growing of inorganic structures directly on organic templates by controlled modification of interfaces has recently emerged as a powerful technique.[4–6] For example, the DRC (dendron rodcoils) nanoribbons were employed as the template in preparing helical cadmium sulfide (CdS).[7] The patterned self-assembled monolayers of alkanethiolates on gold have also been used as the template to synthesize cube-shaped CdS nanoparticles.[3] An aminopyrene-modified carbon nanotube produced by the well-known noncovalent interactions between the pyrenyl groups and the carbon nanotube served as an excellent template to prepare nanoscale CdS clusters and silica nanoparticle hybrids.[8–10] On a PDA-based (PDA: polydiacetylene) Langmuir film, CdS nanoparticles crystallize in the zinc blende structure with a predominant [100]

[a] *Shandong Provincial Key Laboratory of Fluorine Chemistry and Chemical Materials, School of Chemistry and Chemical Engineering, University of Jinan, Jinan, 250022, China. E-mail: chm_chenyl@ujn.edu.cn*
[b] *Department of Chemistry, Shandong University, 250100, China. E-mail: xiyouli@sdu.edu.cn*

† Electronic supplementary information (ESI) available: The energy-optimized conformation of **PDI-1** and **PDI-2** obtained from DFT calculation. π–*A* isotherms of **PDI-1** and **PDI-2** at the air–$CdCl_2$ subphase interface with different $CdCl_2$ concentration after evaporation of CH_2Cl_2 for 3 h, and π–*A* isotherms of **PDI-1** and **PDI-2** at the air–$CdCl_2$ subphase interface with different interaction times between the PDI molecules and Cd^{2+} ions in the 5×10^{-4} mol L^{-1} $CdCl_2$ subphase. SEM images of the Langmuir films of **PDI-1** and **PDI-2** on the pure water surface and $CdCl_2$ subphase surface; *I*–*V* curves of the **PDI-1** and **PDI-2** LS films. The cyclic voltammetry (CV) and differential pulse voltammetry (DPV) curves and experimental data for **PDI-1** and **PDI-2**. The experimental data of X-ray diffraction and fluorescence decay (τ) from **PDI** LS films and CdS–**PDI** composite films. See DOI: 10.1039/c3ce41977k

orientation.[11] Very recently, nucleation of CdS nanocrystals on the red phase of PDA was found to have a size dependent cubic-to-hexagonal transformation.[12]

Perylene tetracarboxylic diimide (**PDI**) derivatives have been extensively and intensively investigated as advanced molecular materials.[13,14] In particular, because of their great potential application as organic semiconductors in different molecular electronic devices, the fabrication of ordered nanostructures of these functional molecular materials has become an attractive research area in the past decade.[15–21] Recently, research interests were aroused by highly ordered supramolecular structures of amphiphilic **PDI** derivatives fabricated by the interfacial self-assembly.[22–25] The resulting **PDI**-based aggregates are highly desired for their potential applications not only as good functional organic materials but also as unique templates to induce the formation of highly ordered inorganic nanocrystals. Consequently, semiconducting **PDI**–CdS organic–inorganic composites in nanoscale should be appealing nano-optoelectronic materials due to the possibility of combining desired properties from both components in one, thus creating new properties that may not be present in each individual material.[26,27] In the present paper, we reported controlled preparation of CdS nanoparticle arrays in Langmuir monolayers of two amphiphilic **PDI** derivatives modified with distinctly different side-chains, *N*,*N*′-di[*N*-amido-3,4,5-tris(2-(2-(2-methoxyethoxy)ethoxy)ethoxy)benzamide]-1,7-di(4-*tert*-butylphenoxy)perylene-3,4;9,10-tetracarboxylic diimide (**PDI-1**) and *N*-amido-3,4,5-tris(2-(2-(2-methoxyethoxy)ethoxy)ethoxy)-benzamide-*N*′-amido-3,4,5-tris(dodecyloxy)benzamide-1,7-di(4-*tert*-butylphenoxy)perylene-3,4;9,10-tetracarboxylate diimide (**PDI-2**) (Scheme 1). By using condensed Langmuir monolayers of amphiphilic **PDI-1** and **PDI-2** molecules as templates, the rose- and petal-shaped CdS–**PDI** nanoparticle arrays with a controllable and tunable size were prepared at the air–water interface. The secondary conformation of side chains attached to the **PDI** rings plays a dominant role in determining the overall shape, size and growth orientations of CdS nanocrystals. Furthermore, the intermolecular electron transfer between **PDI** and CdS in the hybrid composites was studied by using common steady-state and time-resolved methods to monitor fluorescence quenching. In particular, enhanced conductivity was observed for the hybrid nanoparticle arrays relative to a respective single component.

Results and discussion

Pressure–area isotherms of the PDI monolayers

The π–*A* isotherms of the two **PDI** compounds change depending on the $CdCl_2$ concentration in the subphase as well as the interaction time between the **PDI** molecules and Cd^{2+} ions in the subphase (Fig. S1, ESI†). As can be found in Fig. S1,† the π–*A* isotherms for monolayers of both **PDI-1** and **PDI-2** multi-molecule arrays on the 0.5 mM $CdCl_2$ subphase with the interaction time of 3 h between the **PDI** molecules and Cd^{2+} ions showed large compressibility.[28] Fig. 1A and B show the reproducible pressure–area (π–*A*) isotherms of the monolayers for two kinds of **PDI** compounds on the surfaces of pure water and 0.5 mM $CdCl_2$ aqueous solutions for 3 h at room temperature. The stable monolayer can be obtained, having limiting molecular areas (extrapolated to $\pi = 0$ for condensed region) of 3.05 and 1.15 nm^2 per molecule for **PDI-1** and **PDI-2** on the pure water surface, respectively (Fig. 1A and B, solid line). These values are considered to correspond to the mean molecular area of the slipped cofacial **PDI** molecules stacked closely with an "edge-on" configuration in the monolayers (Fig. 1C and D),[29,30] where the long-axis of **PDI** molecules is parallel and perpendicular to the water surface for **PDI-1** and **PDI-2**, respectively, in comparison with the corresponding energy-optimized conformation obtained from DFT calculation (Fig. 1 and Scheme S1, ESI†). This reveals the effect of hydrophilic interaction between the polyoxyethylene side chains of the **PDI** molecule on tuning the molecular orientation in the monolayer. It is also true for two kinds of **PDI** compounds on the $CdCl_2$ subphase, as

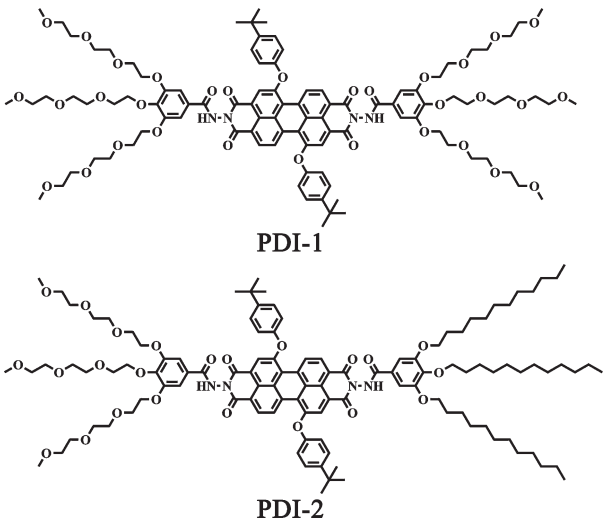

Scheme 1 Schematic molecular structures of **PDI-1** and **PDI-2**.

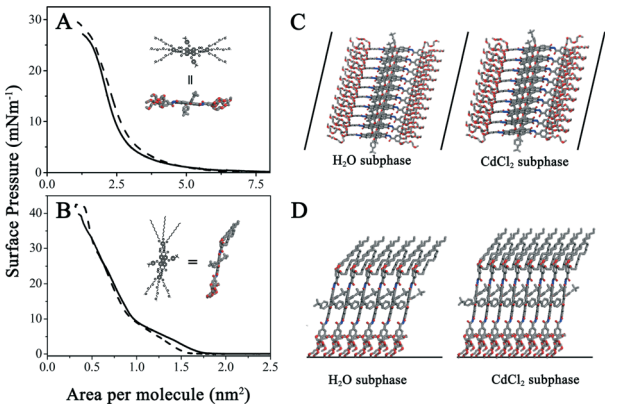

Fig. 1 π–*A* isotherms of **PDI-1** (A) and **PDI-2** (B) on the surface of pure water (solid line) and 0.5 mM $CdCl_2$ aqueous solution (dashed line); schematic arrangement of **PDI-1** (C) and **PDI-2** (D) on the surface of water and $CdCl_2$ aqueous solution. The insets to (A) and (B) show the schematic molecular structure of **PDI-1** and **PDI-2**, respectively.

indicated by π–A isotherms of the monolayers of two **PDI** compounds on the surfaces of $CdCl_2$ aqueous solutions (Fig. 1A and B, dashed line). However, the bigger mean molecular area (3.30 nm^2 per molecule) of **PDI-1** on $CdCl_2$ than that on the pure water subphase (3.05 nm^2 per molecule) suggested the stronger interactions between the **PDI-1** molecules and the Cd^{2+} ions from the $CdCl_2$ subphase. In good contrast, a smaller molecular area (0.91 nm^2 per molecule) of **PDI-2** on the $CdCl_2$ subphase relative to that on the pure water subphase (1.05 nm^2 per molecule) implied the formation of a more compact structure due mainly to the stronger anchoring effect of Cd^{2+} ions between adjacent **PDI-2** molecules associated with the strong hydrophobic interaction among the long dodecyloxy chains of adjacent **PDI-2** molecules in addition to the π–π stacking interaction between the **PDI** rings (Fig. 1D).[30,31] The different molecular packing behaviors of **PDI-1** and **PDI-2** molecules arising from the different side-chain conformations were expected to have a great impact on the crystal growth processes of CdS (*vide infra*).

X-ray diffraction (XRD) pattern

Fig. 2 shows the XRD patterns for CdS nanoparticles formed on **PDI-1** and **PDI-2** Langmuir films collected at different reaction times. For comparison purposes, the XRD patterns of pure **PDI** LS films are also shown in Fig. 2. The corresponding experimental results are compiled in Table S1 (ESI†). In the 2θ range of 20–60°, various diffraction peaks were observed, which were, according to JCPDS file no. 65-3414 (shown as vertical lines in Fig. 2), assigned to the (100), (002), (101), (110) and (112) planes of the hexagonal phase of wurtzite CdS for the nanoparticles formed both on the **PDI-1** film (Fig. 2A) and on the **PDI-2** film (Fig. 2B). However, the (002) diffraction peak of the CdS nanostructures formed on the **PDI-2** film is found to be stronger than expected, whereas a relatively higher intensity of the (101) peak is similar to the literature value for hexagonal wurtzite CdS (JCPDS card no. 65-3414) formed on the **PDI-1** film. Therefore, the preferential growth orientations of the CdS crystalline areas are dependent on which **PDI** templates are used,[32,33] in line with the HRTEM observations (*vide infra*). XRD patterns in combination with SEM and TEM analysis of the samples provided exclusive evidence that rose-/petal-shaped CdS nanoparticles were formed and that the particles exhibit a highly crystalline structure (*vide infra*). It can be clearly seen in the wide angle range of Fig. 2A and B that the broad XRD peaks corresponding to hexagonal wurtzite CdS at different reaction times appeared at almost the same diffraction positions, and this proves the nanocrystalline nature of CdS and a similar crystal morphology for the nanoparticles prepared on the same organic template. On the other hand, in the low angle range, the XRD patterns of both pure **PDI-1** LS films and CdS nanostructures formed on the **PDI-1** film (CdS–**PDI-1** composite films) exhibit the (001) Bragg peak at 2θ = 5.70° and 5.86°–6.04°, respectively, corresponding to a periodic spacing distance of 1.55 and 1.51–1.46 nm for **PDI-1**

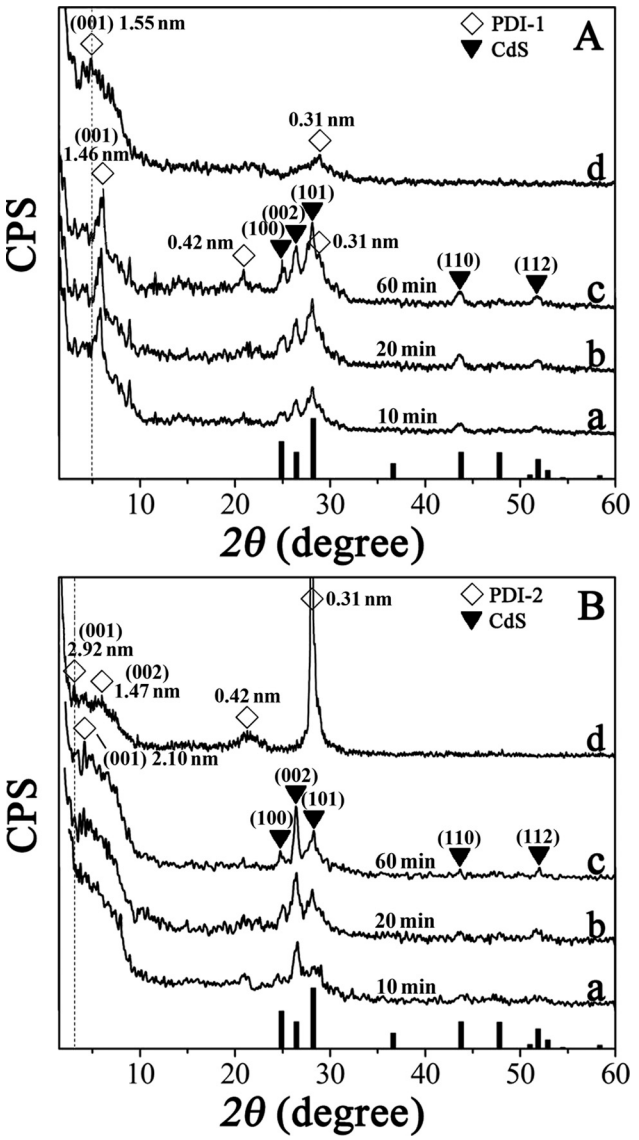

Fig. 2 The X-ray diffraction patterns of CdS nanostructures formed on the Langmuir film of **PDI-1** (A) and **PDI-2** (B), collected at a reaction time of 10 min (line a); 20 min (line b); 60 min (line c), together with the respective pure LS films (line d). The vertical lines show the CdS powder diffraction pattern from Joint Committee on Powder Diffraction Standards (JCPDS) card no. 65-3414.

in the solid films (Fig. 2A). Consequently, orientation angles of **PDI-1** rings with respect to the substrate surface of *ca.* 59.4° and 57.0°–54.2° are estimated for **PDI-1** in pure and composite films based on the width of **PDI-1** (1.80 nm) taken from the energy-optimized structure (Scheme S1, ESI†). A slipped co-facial stacking mode with the molecular long-axis parallel to the substrate surface in an "edge-on" configuration (H aggregate) was achieved for **PDI-1** in either pure or composite film,[34] which is in line with UV–vis absorption and fluorescence spectroscopic studies (*vide infra*). **PDI-2** shows a similar stacking behavior in both its pure and composite films (Fig. 2B). However, a much bigger monolayer thickness (or periodic spacing distance) of **PDI-2** (2.92–2.10 nm) than that of **PDI-1** (1.55–1.46 nm) in either pure or composite film

implies that the molecular long-axis of **PDI-2** is not parallel but perpendicular to the surface of the substrate. The results are well in line with the findings deduced from the *π–A* isotherms, indicating that the orientation and packing structures of **PDI** molecules are determined primarily at the air–liquid interface and do not change significantly from the liquid surface to solid substrates.[35] In addition, in comparison with the XRD pattern of pure **PDI-1** films, the appearance of the (002) diffraction at 1.47 nm and a broad peak at 0.42 nm for pure **PDI-2** films suggested that there exists very regular repetition of the nanostructure along the molecular long-axis of the **PDI-2**,[36] and liquid-like ordered packing of long alkyl chains.[37,38] A stronger and sharper peak at 0.31 nm ($2\theta = 28.9°$) obtained for the **PDI-2** LS films relative to that of the **PDI-1** LS films, which is ascribed to the π–π stacking distance of PDI rings between the adjacent molecule,[39] implied a more favorable molecular packing from a co-facial conformation depending mainly on the π–π interaction between perylene rings in the **PDI-2** films. In the CdS–**PDI-1** composite films, the diffraction peak of **PDI-1** at 0.42 nm grows in intensity along with the increase of reaction time from 10 to 60 min (Fig. 2A). However, in the CdS–**PDI-2** composite film, the diffraction peak at 0.42 nm decreases in intensity along with the increase of the reaction time. This suggests that CdS crystal grown on organic templates has a remarkable influence on the assembly structure of long alkyl chains attached to **PDI** in the composite films.[40,41] As a result, the long hydrophobic alkyl chains of **PDI-2** in the composite film might no longer take an extended conformation but a folded and tangled conformation instead. Consequently, a significant decrease in monolayer thickness of **PDI-2** obtained in the CdS–**PDI-2** composite film as compared to that in the pure **PDI-2** film can be achieved (Fig. 2B). On the other hand, a slightly smaller monolayer thickness of **PDI-1** in the CdS–**PDI-1** composite film than that in the pure film should be attributed to a greater planar conformation of the molecule in the composite film, which is in good agreement with experimental observations from *π–A* isotherms.

Morphology of CdS–PDI nanostructures with controlled size

CdS–**PDI** hybrids were produced *via* CdS nanoparticles formed on **PDI-1** and **PDI-2** Langmuir films at the air–$CdCl_2$ aqueous solution interface after the different reaction times between the Cd^{2+} ions and H_2S gas from 10, 20 to 60 min. The unique CdS nanoparticles were obtained with the diameter gradually increasing from 40, 60 to 80 nm on **PDI-1** Langmuir film, and from 20 to 30 nm on **PDI-2** film after the reaction time from 10, 20 to 60 min, according to the SEM observations (Fig. 3A–F). Surprisingly, upon comparison, we can infer from Fig. 3E and F that the diameter of the nanoparticles formed on the **PDI-2** film did not change significantly by prolonging the reaction time from 20 to 60 min, but it increased the quantity of nanoparticles. This indicates that varying the **PDI** organic template has an even more pronounced influence on the size of CdS nanoparticles than

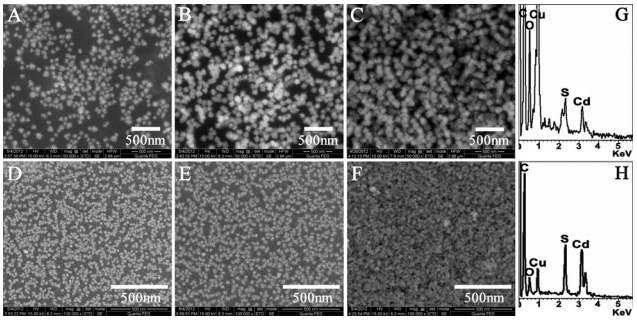

Fig. 3 SEM images of CdS nanoparticles formed on the **PDI-1** Langmuir film (A, B and C) and on the **PDI-2** Langmuir film (D, E and F) collected at a reaction time of 10, 20 and 60 min, respectively. The EDS patterns of CdS nanoparticles formed on **PDI-1** (G) and **PDI-2** (H) Langmuir films after a reaction time of 60 min.

changing the reaction time. The strong hydrophobic interaction among the long alkyl chains of adjacent **PDI-2** molecules together with the close stacking of perylene diimide units render it possible for **PDI-2** molecules to form a compacted film on the subphase surface, which may provide a kinetic barrier to the diffusion of H_2S molecules into the $CdCl_2$ subphase. As a consequence, a relatively low particle growth rate was observed for the formation of CdS nanoparticles at the air–water interface. Furthermore, the elemental composition of both CdS–**PDI-1** and CdS–**PDI-2** composites was examined using an energy dispersive spectroscopy (EDS) analyser attached to an SEM instrument (Fig. 3G and H). The typical EDS spectra from the composites confirmed the presence of C, O, Cd and S. The Cd : S atomic ratio of *ca.* 1 : 1.1 is consistent with our experimental stoichiometric CdS within experimental error,[25] indicating that CdS was adsorbed onto the **PDI** surface. Additional Cu peaks in the spectra originate from the carbon coated Cu grid used as a sample support.

To reveal internal structure and morphology, magnified transmission electron microscopy (TEM) was also employed. As shown in Fig. 4A–B and E–F, the TEM images of CdS nanoparticles formed on **PDI-1** (reaction time: 60 min) and **PDI-2** Langmuir films (reaction time: 20 min) revealed rose- and petal-like morphology with an average diameter of

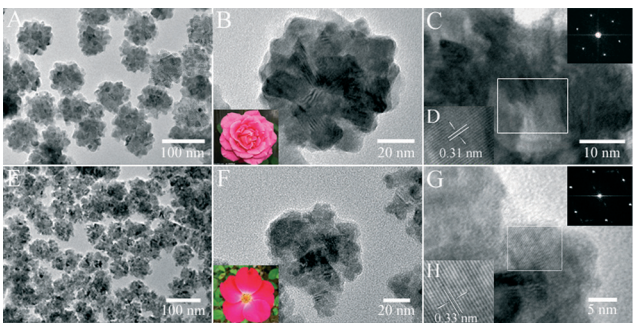

Fig. 4 TEM images of the typical CdS nanoparticles formed on the **PDI-1** Langmuir film (A–B) and on the **PDI-2** Langmuir film (E–F), HRTEM image of individual rose (C–D) and rose petals (G–H). The insets to (C) and (G) show the SAED patterns taken from a rectangular region of the individual nano-rose and nano-rose petals, respectively.

about 80 nm and 30 nm, respectively, which is well consistent with those observed by SEM. The high resolution TEM (HRTEM) images of the individual nano-rose (Fig. 4C and D) and nano-petal (Fig. 4G and H) displayed well-resolved lattice planes with an inter-planar distance of 0.31 and 0.33 nm, which correspond to the (101) and (002) *d*-spacing of the CdS hexagonal (wurtzite) structure, respectively.[42,43] This result obviously suggests that the preferential orientation of the CdS crystalline phase is controlled by the architectures of **PDI** templates. The selected area electron diffraction (SAED) pattern taken from a rectangular region of the individual nano-rose and nano-petal, as shown in the inset of Fig. 4C and G, presents a single-crystal diffraction pattern for either nano-rose or nano-petal, indicating that the CdS nanoparticles are composed of fine hexagonal wurtzite CdS nanocrystals. This result is consistent with that deduced from the XRD experiments.

Formation mechanisms of nanostructures

Crystallization of CdS on the two different **PDI** templates offers precise control of crystal size and shape. The surface morphologies of the **PDI** (**PDI-1** and **PDI-2**) Langmuir films at the air–subphase interface as the nucleating templates were observed by SEM, as shown in Fig. S2 (ESI†). As revealed, the **PDI** films obtained from both water and $CdCl_2$ subphase surfaces exhibited a similar film morphology, which consisted of a granular structure with the diameter of the aggregate domains of *ca.* 300–500 nm. The observations strongly support the previous view (deduced from the π–*A* isotherms of the monolayers) that, in the present **PDI**-based Langmuir film, the packing mode of the molecular assemblies constructed in the $CdCl_2$ subphase is very similar to those formed in the pure water subphase. On the basis of the abovementioned experimental results, the formation mechanism of the nano-roses and nano-petals of CdS–**PDI** nanocomposites was proposed and shown in Fig. 5. First, the formation of well orientated CdS–**PDI** nano-roses and nano-petals should be attributed to a pronounced organic template effect. Associated with the different secondary conformation of the hydrophilic/hydrophobic chain covalently linked to the **PDI** ring in the respective Langmuir film, oriented aggregation of amphiphilic **PDI-1** and **PDI-2** molecules lead to the variable charge densities and micro-structural features in the organic layer (Fig. 5(i)). Once the "cores" (crystal nucleus) are formed through oriented attachment on unique ion-binding sites provided by the **PDI** Langmuir films, they grow larger with reaction time (Fig. 5(ii)). Furthermore, the growth rates of the nano-CdS on **PDI-1** (40–80 nm in diameter in a reaction time of 10–60 min) and **PDI-2** templates (20–30 nm in diameter in a reaction time of 10–60 min) can be controlled through the different micro-channels formed by two kinds of **PDI** templates. In CdS particles formed on the **PDI-2** template by a low rate, the penetration of Cd^{2+} ions through the fine channels of **PDI-2** films, which are composed of less hydrophilic regions (promoting CdS deposition) and more hydrophobic regions (inhibiting growth of CdS nanoparticles by preventing diffusion of both Cd^{2+} ions and H_2S gas molecules to the surfaces of existing nuclei) relative to those of **PDI-1** films, results in the formation of petal-like nanostructures with smaller size (Fig. 5B(iii)). In good contrast, in CdS nanoparticles formed on the **PDI-1** template by a high rate, the penetration of Cd^{2+} ions and diffusion of H_2S molecules through the channels of **PDI-1** films having more hydrophilic groups lead to the formation of rose-like structures with a larger size (Fig. 5A(iii)). Similar examples have been found for two extreme cases of biomineralization, the formation of mollusk shells (a few grams per year) and avian eggshells (5 grams per day), respectively.[44,45] Secondly, primary CdS particles adsorbed on the **PDI** monolayer attach to one another in an irreversible and highly oriented fashion to produce secondary particles that are the unique CdS single crystals. The nanoparticles with wurtzite CdS crystal structure have two basal facets of (001) and (00$\bar{1}$) and six side facets. The two basal facets are composed of either positively charged metal atoms or negatively charged S atoms, respectively, leading to a dipole moment along the [001] axis. It is inferred that (001) facets of the wurtzite CdS nanoparticles would be parallel to the interface between the subphase and air according to their positive nature and the characteristic of the secondary structural conformation of the **PDI-2** molecules in the Langmuir film. It should be mentioned that the CdS nanoparticles have six side facets, which have equal chances to attach their neighboring nanocrystals. Obviously, it is the oriented attachment growth of the nanoparticles along the [001] direction that leads to the formation of CdS nano-petals within the **PDI-2** template. Furthermore, considering the non-polar (101) facets formed by both metal and S atoms, perhaps the greatest selectivity for orientated aggregation along with [101] direction nucleating at an optimized or "engineered" **PDI-1** template surface has a lower energy barrier.

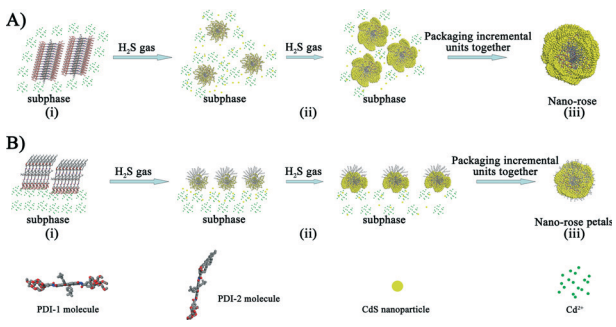

Fig. 5 Schematic illustration of the formation process of CdS–**PDI-1** nano-rose (A) and CdS–**PDI-2** nano-rose petals (B).

UV–vis absorption and fluorescence emission spectra

The UV–vis absorption and corresponding fluorescence emission spectra of the resulting CdS–**PDI-1** and CdS–**PDI-2** composite films are compared (Fig. 6). It can be seen that the edge absorptions of the composite films are coincident with the literature values of CdS nanostructures.[42,46,47] Note that the absorption edge of CdS–**PDI** composite films is blue-shifted

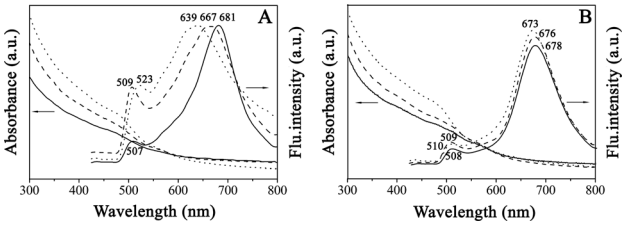

Fig. 6 UV–vis absorption and fluorescence emission spectra (λ_{ex} = 410 nm) of CdS nanostructures formed on **PDI-1** (A) and **PDI-2** (B) Langmuir films collected at a reaction time of 10 min (solid line), 20 min (dashed line) and 60 min (dotted line), respectively.

gradually with decreased reaction time, indicating the formation of smaller CdS nanoparticles on the template of the **PDI** Langmuir film at shorter reaction time.[48] However, we have not observed the absorption peaks from the **PDI** component in the UV–vis absorption CdS–**PDI** composite films, which were expected to appear at *ca.* 517–519 nm (0–1 vibronic band) and *ca.* 550–555 nm (0–0 vibronic band) in comparison with those of pure **PDI** films (Fig. 7).[37,48] It was very likely that the absorption bands of **PDI** films were overlapped by the absorption of CdS nanoparticles because of the stronger absorbance in the wavelength region below 555 nm of CdS in the composite films. Interestingly, the intense emission bands centered at 681–639 nm obtained for the CdS–**PDI** composite films upon excitation at 410 nm disclosed the contribution of the **PDI** component by comparing with that of the **PDI** pure films (centered at 678–689 nm) (Fig. 6 and 7). Furthermore, the red-shifted emission in the longer-wavelength region (681–639 nm), as compared to that in solution of **PDI** (*ca.* 580 nm, Fig. 7), should be attributed to the excimer formed by the interaction between adjacent **PDI** molecules in the slipped cofacial arrangement in H-type aggregation.[37,47,48] Meanwhile, an emission band with relatively weak intensity in the 507–523 nm region can be assigned to the emission of CdS nanostructures.[36,42,46,49] Consistent with the absorption measurement, the emission maxima of CdS also show a gradual blue-shift depending on particle size (Fig. 6). It is worth noting that a comparison of the fluorescence quantum yield (Φ_f) between the LS films of **PDI**s ($\Phi_{fPDI\text{-}1}$ = 0.08 and $\Phi_{fPDI\text{-}2}$ = 0.09) and those in diluted dichloromethane solution ($\Phi_{fPDI\text{-}1}$ = 0.892 and $\Phi_{fPDI\text{-}2}$ = 0.827) by using *N*,*N*-dicyclohexyl-1,7-di(4-*tert*-butyl)phenoxyperylene-3,4;9,10-tetracarboxylate diimide in CH_2Cl_2 as a reference[38] indicated a significant quenching in the former case, due to

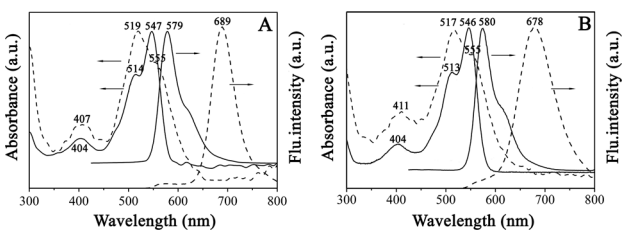

Fig. 7 Normalized UV–vis and fluorescence spectra (λ_{ex} = 410 nm) of **PDI-1** (A) and **PDI-2** (B) in dichloromethane solution of 5×10^{-6} mol L^{-1} (solid line) and LS films fabricated at the air–water interface (dashed line).

the formation of **PDI** aggregates. This finding is consistent with electronic coupling between the **PDI** cores formed by the interaction between adjacent **PDI** molecules in a slipped co-facial arrangement.[50]

Electron transfer in CdS–PDI composite films

Considering a larger contribution to the emission from the **PDI** component detected in this particular CdS–**PDI** nanocomposite, intermolecular interaction between CdS and **PDI** was studied by monitoring the steady-state and transient fluorescence decay at the emission peak of the **PDI** (λ_{ex} = 520 nm) (Fig. 8). As can be seen from Fig. 8A and B, upon attachment to the CdS nanocrystals, the fluorescence of the **PDI** is quenched *ca.* 97% and 87% for **PDI-1** and **PDI-2**, respectively, suggesting that a photoinduced electron-transfer has occurred from the **PDI** molecules to CdS nanoparticles. This has become possible due to well separated emission peaks of CdS (507–523 nm) and **PDI** (681–639 nm), enabling the selective excitation of only the **PDI** in a hybrid and no spectral overlap between the emission band of **PDI** and the absorption band of CdS. Furthermore, the type II band alignment of the HOMO and LUMO levels of **PDI** and CdS nanoparticles makes evident the possibility of charge separation (Scheme 2),[51,52] where the absolute positions of the LUMO (−3.9 to −3.95 eV) and HOMO (−5.96 to −5.98 eV) levels of the **PDI** were determined by cyclic voltammetry (CV) and differential pulse voltammetry (DPV) (Fig. S1 and Table S2, ESI†). The conduction band (E_c, −4.1 eV) and valence band (E_v, −6.5 eV) of CdS are known.[25] When **PDI** molecules are excited, electrons of the **PDI** can be excited from its HOMO to LUMO level, while the photoexcited electron at the LUMO energy level of the **PDI** can easily transfer to the E_c band of close-by CdS nanocrystals (Scheme 2) since the energy levels of **PDI**

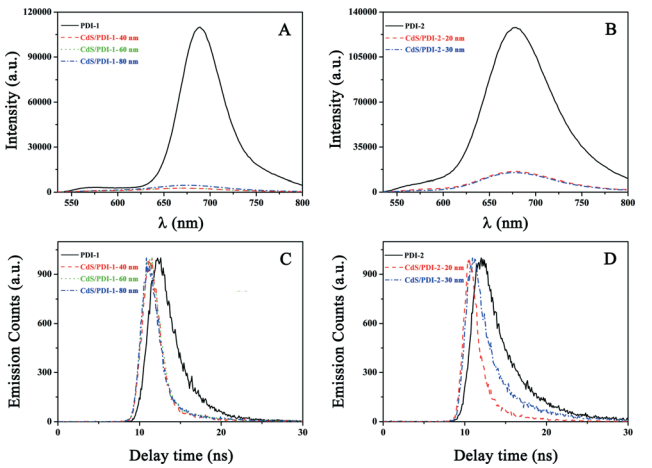

Fig. 8 The fluorescence emission spectra (top) and fluorescence decay (bottom) of **PDI-1** (A and C) and **PDI-2** (B and D) LS films (black solid line) and the corresponding CdS–**PDI** composites with particle sizes of 40 nm (red dashed line), 60 nm (green dotted line) and 80 nm (blue dash-dotted line) for CdS–**PDI-1** (A and C); 20 nm (red dashed line) and 30 nm (blue dash-dotted line) for CdS–**PDI-2** (B and D), respectively. (λ_{ex} = 520 nm).

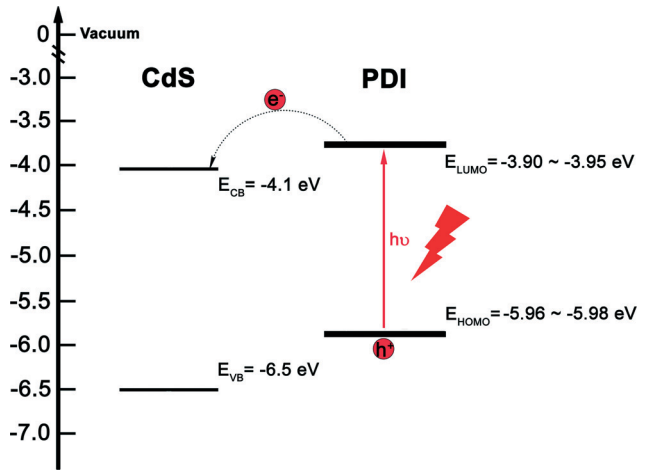

Scheme 2 Electron-transfer mechanism from **PDI** to CdS nanocrystals.

(HOMO and LUMO) and CdS (E_v and E_c) are compatible for electron transfer with the **PDI** molecule as the donor and the CdS nanoparticle as the acceptor. The photoinduced electron-transfer from the **PDI** molecules to the CdS nanoparticles is further supported by lifetime measurements. Transient fluorescence decay of **PDI** without and with CdS linkage was monitored at the emission peak of the **PDI**, and the data are compiled in Table S3 (ESI†) and Fig. 8. For the pure **PDI-1** and **PDI-2** LS films, the lifetime measurements obtained were 2.91 and 3.50 ns, respectively, which match well with the reported values.[53] We recover a two component exponential population decay for all of the different particle sizes of these particular donor/acceptor hybrid systems, with time constants of 1.20–1.57 ns (86–90%) and 11.24–10.10 ns (10–14%) for CdS–**PDI-1** composites and 1.40–2.50 ns (92–82%) and 17.30–10.20 ns (8–18%) for CdS–**PDI-2** composites. The dominant effect we observe is the reduction in lifetime associated with attachment of the CdS nanocrystals to the **PDI** chromophores, which unambiguously confirms ultrafast electron-transfer from **PDI** molecules to CdS nanocrystals, indicating a strong interaction between **PDI** molecules and the close-by CdS nanocrystals.

Semiconducting properties of CdS–PDI composites

The size/shape-dependent semiconducting properties of CdS–**PDI-1** nano-roses and CdS–**PDI-2** nano-petals are obtained by current–voltage (*I–V*) measurement (Fig. 9). According to the equation reported in the literature,[54] the electronic conductivity of the nano-roses with an increased average diameter of *ca.* 40, 60 and 80 nm is calculated to be around 2.4×10^{-7}, 1.1×10^{-6} and 7.6×10^{-5} S cm^{-1}, respectively, which is about 1–3 orders of magnitude larger than that of the nano-petals with an average diameter of *ca.* 20 nm and 30 nm (*ca.* 1.1×10^{-8} and 8.8×10^{-8} S cm^{-1}, respectively). The larger and more uniform nano-grain sizes for nano-roses compared to those of nano-petals are expected to cause fewer traps and/or defects localized around grain boundaries, thus improving the carrier mobility.[55–57] It should be noted that the *I–V*

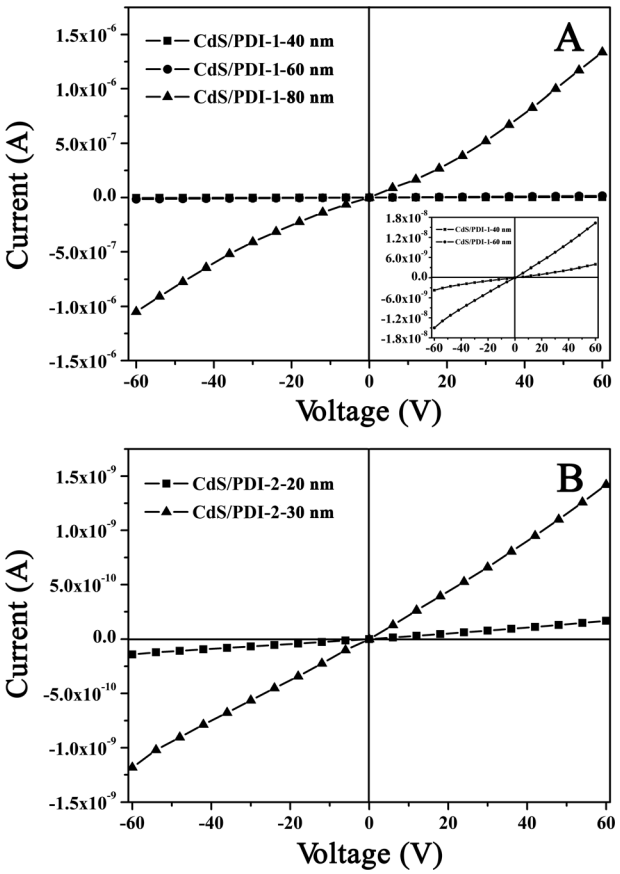

Fig. 9 *I–V* curves of the composites with particle sizes of 40 nm (■), 60 nm (●) and 80 nm (▲) for CdS–**PDI-1** (A); 20 nm (■), and 30 nm (▲) for CdS–**PDI-2** (B), respectively. The inset is the magnified *I–V* curves of CdS–**PDI-1** composites of 40 and 60 nm.

characteristics of pure **PDI-1** and **PDI-2** LS films were also investigated comparatively, and the conductivities of two kinds of films are in the range of ~10^{-9} S cm^{-1} (Fig. S2, ESI†), while the conductivity of bulk CdS crystals is around ~10^{-10} S cm^{-1} as reported previously.[58,59] Consequently, an enhanced conductivity for both nano-roses and nano-petals of CdS–**PDI** hybrid nanocomposites was achieved, relative to that of either the bulk CdS crystals or pure **PDI** components, which was interpreted in terms of the existence of the densely packed molecular architecture in the film matrix and the large interfacial area between the CdS and **PDI** components that removed the charge transporting bottleneck by creating an interpenetrating network of the hybrid materials. It is noteworthy that these nanostructures with relatively high current modulation should be useful for a wide range of electronic and sensor devices. The efforts to explore such opportunities are underway.

Conclusions

Two amphiphilic **PDI** derivatives modified with distinctly different side-chains can form a very stable monolayer on the surface of both water and $CdCl_2$ aqueous solution. Due to the different hydrophobic/hydrophilic side-chains attached to

the **PDI** ring, the self-assembly of the two **PDI** molecules in the Langmuir film presents a different structure. By using the resulting films as organic templates, the highly uniform CdS–**PDI** nano-particles with a controllable and tunable size (from 40 to 80 nm for nano-roses; from 20 to 30 nm for nano-petals) were prepared. In particular, the different preferred [101] and [001] orientations of the hexagonal wurtzite CdS nanocrystallites were found to form on the **PDI-1** or **PDI-2** template, respectively, which can be rationalized in terms of the secondary structural conformation of the **PDI** organic template employed and the oriented attachment of hexagonal CdS nanocrystals. The results provide new insights into the organic template–mineral interaction for synthesizing CdS–**PDI** inorganic–organic nanoparticles under mild conditions. It also suggests that the controllable growth of the nanoparticles with a different exposure facet by engineering the organic template is practical. Particularly, in hybrid nanocomposites of semiconductor **PDI** and CdS nanocrystals, with type-II alignment of HOMO and LUMO levels, electron-transfer from a number of **PDI** molecules to CdS nanocrystals is established, depending on the **PDI**–CdS interaction. Furthermore, the electronic conductivity of CdS–**PDI** hybrid nanoparticles significantly increased with the increase in average particle size from 20 nm to 80 nm. An especially high conductivity (~7.6×10^{-5} S cm^{-1}) is achieved by the CdS–**PDI** nano-roses of 80 nm, which is about 3 orders of magnitude larger compared to the value of ~1.1×10^{-8} S cm^{-1} of the conductivity of the nano-petals of 20 nm. The present result represents the first effort towards controlling and tuning the size and morphology and in particular the growth orientations of CdS nanostructures *via* tuning the secondary conformation of polyoxyethylene side chains covalently linked to the **PDI** rings, which is helpful towards designing and preparing new nanomaterials and more complex nanostructures with tunable functionality.

Experimental section

Chemicals

The samples of **PDI-1** and **PDI-2** were synthesized according to previously published procedures.[37] $CdCl_2 \cdot 2.5H_2O$ and $Na_2S \cdot 9H_2O$ were purchased from Shanghai Chemical Reagent Co. All the chemicals are analytical reagents and used without further purification.

Formation and characterization of the nanostructures

An aqueous solution of $CdCl_2$ (5×10^{-4} mol L^{-1}) in ultrapure water with resistivity greater than 18 MΩ cm^{-1} was used as the subphase (pH = 5.5). Two beakers filled with the subphase and the Na_2S aqueous solution that was used to produce H_2S gas, respectively, were placed in a sealed 7.8 L container. The Langmuir monolayer of **PDI-1** and **PDI-2** was formed by spreading 5.0 μL 1.60×10^{-4} mol L^{-1} **PDI-1** and 30 μL 1.09×10^{-4} mol L^{-1} **PDI-2** dichloromethane solution onto the 5×10^{-4} mol L^{-1} $CdCl_2$ aqueous solution surface of 12.6 cm^2, respectively. The mean molecular area was calculated to be 2.60 nm^2 and 0.64 nm^2, respectively, which corresponds to the molecular area at the onset of the closely packed liquid-condensed phase in the respective π–A isotherm obtained from Langmuir trough (NIMA 622, Great Britain). After evaporating the organic solvent for a different time, 3 h, H_2SO_4 was poured into the Na_2S aqueous solution to produce H_2S and the container was sealed immediately. The initial concentration of H_2S was controlled by the amount of Na_2S. After reaction for various reaction times from 10, 20 to 60 min, the monolayer was transferred onto carbon coated copper grids and quartz slides by the Langmuir–Shäfer (LS: horizontal transfer) method, for SEM (Hitachi S-4300 F), TEM (JEM-100CXII), HRTEM (GEOL-2010), EDS (Oxford INCA X-sight), X-ray diffraction (Rigaku D/max-γB), fluorescence (FLS920) and UV–vis spectroscopy (Hitachi U-4100) measurements, respectively. Solid-state emission spectra as well as luminescence lifetime measurements were carried out using an Edinburgh FLS920 phosphorimeter equipped with a continuous Xe-900 xenon lamp and an nF900 ns flash lamp. The emission quantum yields of the LS films of **PDI-1** and **PDI-2** were measured at room temperature using a calibrated integrating sphere as a sample chamber, and Specpure $BaSO_4$ was used as a reflecting standard, while those of **PDI-1** and **PDI-2** in diluted dichloromethane solution were obtained by using *N*,*N*-dicyclohexyl-1,7-di(4-*tert*-butyl)phenoxyperylene-3,4;9,10-tetracarboxylate diimide in CH_2Cl_2 as a reference.[38] The reactions were carried out at room temperature. The LS films of **PDI-1** and **PDI-2** were deposited onto quartz substrates for X-ray diffraction, UV–vis, and fluorescence spectra measurement by LS method while the surface pressure was kept at 20 and 30 mN m^{-1}, respectively. The time interval between two consecutive layer depositions was 15 min.

Device fabrication

A 20 nm-thick gold interdigitated electrode (IDE) array composed of 6 pairs of Au electrode digits was deposited on a SiO_2/Si substrate *via* a shadow mask. The interelectrode spacing and overlapping length of the IDE were 0.24 and 2.60 mm, respectively. Subsequently, either pure **PDI** films or CdS–**PDI** nano-composites (20-layer) were deposited onto a SiO_2/Si substrate with IDE by the LS method, respectively. The current–voltage characteristics were obtained by using a Keithley 4200 semiconductor characterization system at room temperature in air. All experiments have been conducted at least twice to ensure reproducibility. The conductivity, σ, can be calculated according to the reported methods in the previous literature.[54]

Acknowledgements

The authors would like to thank the Natural Science Foundation of China (21371073, 21073112) and the Natural Science Foundation of Shandong Province (ZR2011BZ005) for the financial support of this work.

Notes and references

1 A. P. Alivisatos, *Science*, 1996, **271**, 933.
2 J. H. Zhan, X. G. Yang, D. W. Wang, S. D. Li, Y. Xie, Y. Xia and Y. Qian, *Adv. Mater.*, 2000, **12**, 1348.
3 C. C. Chen and J. J. Lin, *Adv. Mater.*, 2001, **13**, 136.
4 A. Vilan and D. Cahen, *Trends Biotechnol.*, 2002, **20**, 22.
5 K. J. C. Van Bommel, A. Friggeri and S. Shinkai, *Angew. Chem., Int. Ed.*, 2003, **42**, 980.
6 Y. Lu, Y. Yang, A. Sellinger, M. Lu, J. Huang, H. Fan, R. Haddad, G. Lopez, A. R. Burns, D. Y. Sasaki, J. Shelnutt and C. J. Brinker, *Nature*, 2001, **410**, 913.
7 E. D. Sone, E. R. Zubarev and S. I. Stupp, *Angew. Chem., Int. Ed.*, 2002, **41**, 1705.
8 R. J. Chen, Y. Zhang, D. Wang and H. Dai, *J. Am. Chem. Soc.*, 2001, **123**, 3838.
9 L. Liu, T. Wang, J. Li, Z. X. Guo, L. Dai, D. Zhang and D. B. Zhu, *Chem. Phys. Lett.*, 2003, **367**, 747.
10 X. L. Li, Y. Q. Liu, L. Fu, L. C. Cao, D. C. Wei and Y. Wang, *Adv. Funct. Mater.*, 2006, **16**, 2431.
11 Y. Lifshitz, O. Konovalov, N. Belman, A. Berman and Y. Golan, *Adv. Funct. Mater.*, 2006, **16**, 2398.
12 A. Upcher, V. Ezersky, A. Berman and Y. Golan, *Nanoscale*, 2012, **4**, 7655.
13 F. Würthner, *Chem. Commun.*, 2004, 1564.
14 H. Langhals, *Helv. Chim. Acta*, 2005, **88**, 1309.
15 L. S. Mende, A. Fechtenkötter, K. Müllen, E. Moons, R. H. Friend and J. D. MacKenzie, *Science*, 2001, **293**, 1119.
16 B. A. Gregg, *J. Phys. Chem. B*, 2003, **107**, 4688.
17 G. Tamizhmani, J. P. Dodelet, R. Cote and D. Gravel, *Chem. Mater.*, 1991, **3**, 1046.
18 E. Peeters, H. P. A. Van, S. C. J. Meskers, R. A. J. Janssen and E. W. Meijer, *Chem.–Eur. J.*, 2002, **8**, 4470.
19 J. Locklin, D. Li, S. C. B. Mannsfeld, E. J. Borkent, H. Meng, R. Advincula and Z. Bao, *Chem. Mater.*, 2005, **17**, 3366.
20 C. W. Struijk, A. B. Sieval, J. E. J. Dakhorst, D. M. Van, P. Kimkes, R. B. M. Koehorst, H. Donker, T. J. Schaafsma, S. J. Picken, C. A. M. Van, J. M. Warman, H. Zuilhof and E. J. R. Sudhölter, *J. Am. Chem. Soc.*, 2000, **122**, 11057.
21 S. Yin, B. Song, G. Liu, Z. Wang and X. Zhang, *Langmuir*, 2007, **23**, 5936.
22 Y Chen, Y. Kong, Y. Wang, P. Ma, M. Bao and X. Li, *J. Colloid Interface Sci.*, 2009, **330**, 421.
23 Y. Wang, Y. Chen, R. Li, S. Wang, W. Su, P. Ma, M. R. Wasielewski, X. Li and J. Jiang, *Langmuir*, 2007, **23**, 5836.
24 N. An, Y. Shi, J. Feng, D. Li, J. Gao, Y. Chen and X. Li, *Org. Electron.*, 2013, **14**, 1197.
25 Y. Chen, L. Chen, G. Qi, H. Wu, Y. Zhang, L. Xue, P. Zhu, P. Ma and X. Li, *Langmuir*, 2010, **26**, 12473.
26 Z. Xu, C. R. Hine, M. M. Maye, Q. Meng and M. Cotlet, *ACS Nano*, 2012, **6**, 4984.
27 J. H. Bang and P. V. Kamat, *ACS Nano*, 2011, **5**, 9421.
28 (*a*) D.-J. Qian, C. Nakamura and J. Miyake, *Langmuir*, 2000, **16**, 9615; (*b*) Q. Liu, Q. Zhao, Y. Li and X. Wang, *CrystEngComm*, 2012, **14**, 1105; (*c*) F. Xiao, H.-G. Liu, C.-W. Wang, Y.-Ill. Lee, Q. Xue, X. Chen, J. Hao and J. Jiang, *Nanotechnology*, 2007, **18**, 435603.
29 G. A. Schick, I. C. Schreiman, R. W. Wagner, J. S. Lindsey and D. F. Bocian, *J. Am. Chem. Soc.*, 1989, **111**, 1344.
30 J. M. Kroon, E. J. R. Sudhoelter, A. P. H. J. Schenning and R. J. M. Nolte, *Langmuir*, 1995, **11**, 214.
31 G. Xu, N. Yao, I. A. Aksay and J. T. Groves, *J. Am. Chem. Soc.*, 1998, **120**, 11977.
32 P. Yan, Y. Xie, Y. Qian and X. Liu, *Chem. Commun.*, 1999, 1293.
33 Y. Li, H. Liao, Y. Ding, Y. Fan, Y. Zhang and Y. Qian, *Inorg. Chem.*, 1999, **38**, 1382.
34 M. Kasha, H. R. Rawls and M. A. E. Bayoumi, *Pure Appl. Chem.*, 1965, **11**, 371.
35 (*a*) H.-G. Liu, D. J. Qian, X. S. Feng, Q. B. Xue and K. Z. Yang, *Langmuir*, 2000, **16**, 5079; (*b*) Y. Chen, H. G. Liu, P. Zhu, Y. Zhang, X. Wang, X. Li and J. Jiang, *Langmuir*, 2005, **21**, 11289.
36 H. Zhao and E. P. Douglas, *Chem. Mater.*, 2002, **14**, 1418.
37 H. Wu, L. Xue, Y. Shi, Y. Chen and X. Li, *Langmuir*, 2011, **27**, 3074.
38 F. Würthner, C. Thalacker, S. Diele and C. Tschierske, *Chem.–Eur. J.*, 2001, **7**, 2245.
39 G. Klebe, F. Graser, E. Hadicke and J. Berndt, *Acta Crystallogr., Sect. B: Struct. Sci.*, 1989, **45**, 69.
40 N. P. Kumar, S. Major, S. Vitta, S. S. Talwar, P. Dubcek, H. Amenitsch, S. Bernstorff, V. Ganesan, A. Gupta and B. A. Dasannacharya, *Colloids Surf., A*, 2002, **198**, 75.
41 P. K. Nayak, S. S. Talwar, S. S. Major and R. S. Srinivasa, *Colloids Surf., A*, 2006, **284**, 187.
42 B. Liu and H. C. Zeng, *J. Am. Chem. Soc.*, 2005, **127**, 18262.
43 S. Acharya, I. Patla, J. Kost, S. Efrima and Y. Golan, *J. Am. Chem. Soc.*, 2006, **128**, 9294.
44 K. Simkiss, Calcium Metabolism and Avian Reproduction *Biol. Rev.*, 1961, **36**, 321.
45 A. Heuer, D. Fink, V. Laraia, J. Arias, P. Calvert, K. Kendall, G. Messing, J. Blackwell, P. Rieke and D. Thompson, *Science*, 1992, **255**, 1098.
46 L. Spanhel, M. Haase, H. Weller and A. Henglein, *J. Am. Chem. Soc.*, 1987, **109**, 5649.
47 Y. Türker, C. Karakaya and Ö. Dag, *Chem.–Eur. J.*, 2012, **18**, 3695.
48 Y. Chen, Y. Feng, J. Gao and M. Bouvet, *J. Colloid Interface Sci.*, 2012, **368**, 387.
49 J. J. J. M. Donners, R. Hoogenboom, A. P. H. J. Schenning, P. A. van Hal, R. J. M. Nolte, E. W. Meijer and N. A. J. M. Sommerdijk, *Langmuir*, 2002, **18**, 2571.
50 (*a*) J. Feng, Y. Zhang, C. Zhao, R. Li, W. Xu, X. Li and J. Jiang, *Chem.–Eur. J.*, 2008, **14**, 7000; (*b*) A. You, J. Gao, D. Li, M. Bouvet and Y. Chen, *Supramol. Chem.*, 2012, **24**, 851.
51 S. S. Lo, T. Mirkovic, C.-H. Chuang, C. Burda and G. D. Scholes, *Adv. Mater.*, 2011, **23**, 180.
52 A. A. Lutich, G. Jiang, A. S. Susha, A. L. Rogach, F. D. Stefani and J. Feldmann, *Nano Lett.*, 2009, **9**, 2636.
53 C. Devadoss, P. Bharathi and J. S. Moore, *J. Am. Chem. Soc.*, 1996, **118**, 9635.

54 Y. Chen, M. Bouvet, T. Sizun, Y. Gao, C. Plassard, E. Lesniewska and J. Jiang, *Phys. Chem. Chem. Phys.*, 2010, **12**, 12851.
55 K. Szendrei, F. Cordella, M. V. Kovalenko, M. Böberl, G. Hesser, M. Yarema, D. Jarzab, O. V. Mikhnenko, A. Gocalinska, M. Saba, F. Quochi, A. Mura, G. Bongiovanni, P. W. M. Blom, W. Heiss and M. A. Loi, *Adv. Mater.*, 2009, **21**, 683.
56 T. Lee, C. A. Landis, B. M. Dhar, B. J. Jung, J. Sun, A. Sarjeant, H. J. Lee and H. E. Katz, *J. Am. Chem. Soc.*, 2009, **131**, 1692.
57 Y. Chen, D. Li, N. Yuan, J. Gao, R. Gu, G. Lu and M. Bouvet, *J. Mater. Chem.*, 2012, **22**, 22142.
58 M. Abdulkhadar and B. Thomas, *Nanostruct. Mater.*, 1998, **10**, 593.
59 C. Elbaum, *Phys. Rev. Lett.*, 1974, **32**, 376.

